



Effect Mechanism of Splitter Blade Length on the Energy Performance of Centrifugal Pump

Q. Ma^{1,2,3,4†}, Z. Liu⁴ and S. Jiang⁵

¹ School of Mechanical Engineering, Hefei University of Technology, Hefei 230009, China

² School of Mechanical and Electrical Engineering, Chuzhou University, Chuzhou 239000, China

³ Anhui Liuxiang Special Ship Co., Ltd., Mingguang 239400, China

⁴ National Research Center of Pumps, Jiangsu University, Zhenjiang 212013, China

⁵ Ningbo Yi Ji Valve Manufacturing Co., Ltd., Ningbo 315528, China

†Corresponding Author Email: qjima@chzu.edu.cn

ABSTRACT

This study integrates numerical simulation and experimental validation to thoroughly examine the effects of splitter blades and their lengths on the energy performance of centrifugal pumps. The results demonstrate that numerical simulations closely align with experimental data in terms of head and efficiency, with an error margin of less than 5%, underscoring the accuracy and reliability of the simulations. Further analysis reveals that centrifugal pumps equipped with splitter blades display distinct performance characteristics compared to conventional impellers, particularly under low-flow conditions. The head curve of pumps with splitter blades exhibits a pronounced extremum and a positive slope in the low-flow region. Splitter blades play a crucial role in enhancing the head performance of centrifugal pumps, effectively expanding their high-head operating range. However, this improvement is accompanied by some efficiency loss, primarily due to fluid kinetic energy losses within the impeller and volute, as well as the structural design of the splitter blades. This research offers valuable theoretical insights and data to support the hydraulic design optimization of centrifugal pumps.

Article History

Received December 16, 2024

Revised March 17, 2025

Accepted April 6, 2025

Available online June 3, 2025

Keywords:

Centrifugal pump

Numerical simulation

Splitter blade

Entropy production loss

Blade length

1. INTRODUCTION

Centrifugal pumps are critical components in diverse industrial and engineering applications (Pu et al., 2024a), including water supply (Pu et al., 2024b), chemical processing (Ji et al., 2024), and power generation (Li et al., 2024a). The performance of these pumps, defined by key parameters such as efficiency, head, and flow rate, is strongly influenced by the geometric design of their impellers (Ji et al., 2024). Among various design strategies, the integration of splitter blades—shorter blades positioned between primary impeller blades—has emerged as a proven method for improving pump performance by reducing flow instabilities and enhancing energy transfer (Ji et al., 2023). This approach is especially valuable in high-specific-speed pumps, where flow irregularities such as large secondary flows, uneven velocity distributions, and energy losses are common (Jin et al., 2023). Splitter blades mitigate these issues by redistributing the flow more uniformly, reducing separation zones, and enhancing hydraulic performance (Kergourlay et al., 2007). However, their effectiveness

depends not only on their presence but also on critical geometric factors, including their length, radial position, and angular orientation relative to the main blades.

Research has highlighted the significance of splitter blade length in determining its impact on pump performance. Namazizadeh et al. (2020) studied the effect of varying splitter blade lengths on centrifugal pump performance by modifying the impeller geometry and adding two different splitter blade lengths for comparison. Their findings revealed that longer splitter blades increased the total head due to enhanced energy transfer but led to higher friction losses, reducing overall efficiency. Similarly, Miyamoto et al. (1992, 1989a, b) analyzed the effects of splitter blades on flow and performance by examining velocity and pressure distributions in shrouded and unshrouded impellers. In their study, splitter blades measuring approximately 60% of the primary blade length were tested. Impellers equipped with these blades exhibited reduced blade loading and significantly higher absolute circumferential velocities and total pressures compared to those without splitter blades. These studies collectively suggest that

longer splitter blades can improve energy transfer but may introduce additional hydraulic losses due to increased blockage and secondary flow effects. Conversely, shorter splitter blades may fail to adequately influence the flow field, limiting performance gains. The optimal splitter blade length for a given centrifugal pump impeller remains an unresolved design challenge. Thus, understanding the mechanisms by which splitter blade length affects centrifugal pump performance is crucial for achieving optimal impeller design and maximizing operational efficiency.

In addition to length, the interaction between splitter blades and primary blades generates complex flow dynamics within the impeller (Shigemitsu et al., 2013). The splitter blades modify the pressure distribution along the primary blades, leading to changes in flow separation and secondary flow patterns (Ye et al., 2012). Their presence also alters the wake region (Fatahian et al., 2022) and the mixing processes within the flow, which significantly impacts the pump's efficiency and cavitation characteristics (Chabannes et al., 2021). Computational Fluid Dynamics (CFD) simulations and experimental studies have been extensively used to examine these interactions (Zhu et al., 2013; Clark et al., 2017; Liang et al., 2023), providing critical insights into the underlying mechanisms. Gölcü et al. (2007) conducted numerical and experimental studies on the effect of splitter blade length on deep well pump performance. They observed that when splitter blades were incorporated, the impeller's exit passages narrowed with an increasing number of impellers. However, positive effects from the splitter blades were not evident in impellers with higher blade counts and discharge angles. Additionally, Zhang et al. (2020) used numerical simulations to compare the influence of splitter blade deflection on the performance of low-specific-speed pumps under various flow rates. They found that the impeller design featuring optimal splitter blade deflection minimized turbulence intensity and ensured a favorable relative velocity distribution within the main flow passage. Further research by Wang et al. (2020), Dong et al. (2024), and Djebedjian (2020), along with contributions from notable scholars (Siddique et al., 2022; Hu et al., 2023; Yu et al., 2023), has emphasized the importance of splitter blades in enhancing the performance of rotating machinery, including pumps, turbines, and fans.

Despite significant advancements, several knowledge gaps persist. One unresolved issue is determining the optimal splitter blade length for various operating conditions and pump designs (Song et al., 2020). Moreover, limited understanding exists regarding how splitter blade length interacts with other design parameters, such as blade count (Siddique et al., 2022), blade angle (Khalafallah et al., 2021), and blade thickness (Xu et al., 2022). Addressing these gaps necessitates a systematic approach involving experimental validation and high-fidelity numerical simulations to comprehensively explore the parametric effects of splitter blade length on pump performance.

This study aims to elucidate the impact of splitter blade length on the performance mechanisms of



Fig. 1 Physical centrifugal pump model

centrifugal pumps. Through detailed analysis of flow characteristics, pressure distributions, and energy conversion processes, the research seeks to optimize splitter blade design to enhance pump efficiency and reliability. The findings are expected to contribute to the development of design guidelines for impellers with splitter blades, enabling improved performance across diverse applications.

2 PHYSICAL MODEL

2.1 Pump Model and Splitter Blade Structure

In this study, we select the ISG25-220 single-stage, single-suction horizontal centrifugal pump as the research subject, as depicted in Fig. 1. The pump's design specifications include a flow rate (Q) of 88 m³/h, a head (H) of 12 m, and a speed (n) of 1450 rpm. A high-efficiency centrifugal pump model with a similar specific speed is employed in designing the pump's hydraulic structure, with the specific speed calculated as follows:

$$n_s = \frac{3.65n\sqrt{Q}}{H^{3/4}} = 21 \quad (1)$$

Two design schemes, one with and one without splitter blades, are compared in this study. To further investigate the impact of splitter blade length on the pump's hydraulic performance, two different splitter blade lengths are examined. Consequently, three impeller hydraulic design schemes are finalized, as illustrated in Fig. 2.

This study primarily employs the rotary bias method in designing the shunt blade. The original non-shunt impeller contains six blades with a 60° angle interval between each blade. To design the split blade, the original blade is rotated by 30°, and its inlet edge is truncated, leaving only the blade's trailing section. The shunt blade length is set to 0.7 and 0.3 times the length of the original blade, respectively. The main parameters of the centrifugal pump model and the diverter blade are detailed in Table 1.

2.2 Pre-Processing of Numerical Calculation

Before performing numerical simulations, some preparatory steps are necessary for the centrifugal pump model. First, the computational domain is modeled using 3D design software. The hydraulic components of the pump—including the inlet, outlet, impeller, volute, and pump gap chamber—are modeled in three dimensions

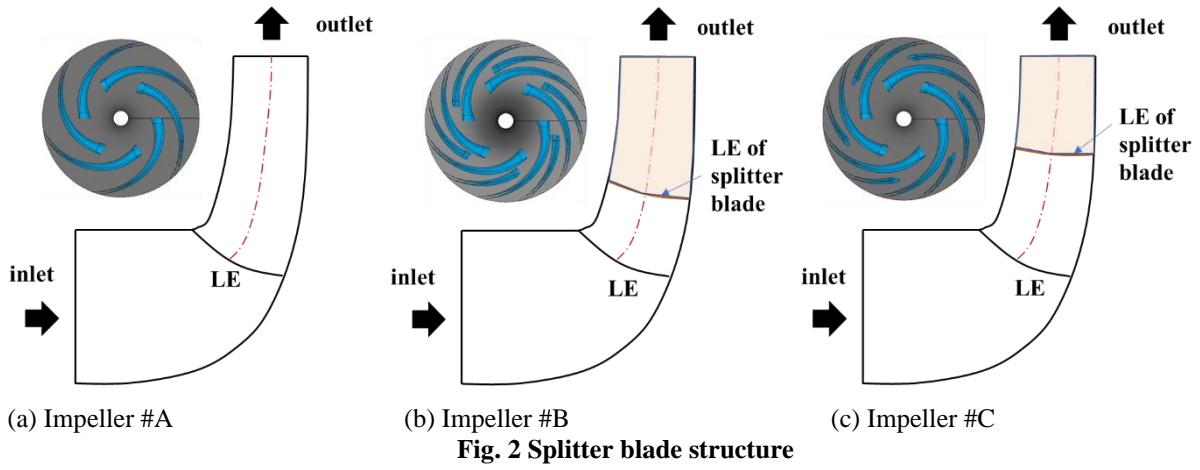


Table 1 Main parameters of the centrifugal pump model

Parameter	Value
Designed flow rate Q_d (m ³ /h)	88
Designed rated head H (m)	12
Rated speed n (rev/min)	1450
Impeller inlet diameter D_1 (mm)	112.5
Impeller outer diameter D_2 (mm)	219
Number of blades Z	6
Impeller outlet width b_2 (mm)	22.02
Blade inlet angle β_1 (°)	
Blade outlet angle β_2 (°)	16.5
Blade wrap angle ϕ (°)	90
Guide vane angle α (°)	15
Volute base circle diameter D_3 (mm)	176.5
Volute outlet diameter D_4 (mm)	100

using UG NX software. In all design schemes presented, the impeller mouth ring clearance is uniform and minimally affects the flow field in the shunt impeller, allowing it to be ignored during modeling. To address potential calculation divergence due to inlet and outlet reflux, the impeller’s inlet and outlet regions are appropriately extended (Gu et al., 2024). The 3D water structure of the centrifugal pump is illustrated in Fig. 3.

Mesh generation is crucial for simulation accuracy and efficiency (Li et al., 2023). In this study, ANSYS ICEM is used to create a hexahedral mesh for most regions. The computational domain is discretized using a mixed mesh approach: structured hexahedral meshes are applied to the inlet, outlet, volute, and pump cavity. This configuration ensures precise control over streamline distribution and boundary layer orthogonality, while allowing for flexible node spacing to refine the boundary layer mesh (Li et al., 2024b). Due to the impeller’s complex hydraulic geometry, a tetrahedral unstructured mesh is used for this component. For consistency, all three impeller schemes utilize the same mesh generation criteria, with a final mesh quality exceeding 0.5. Figure 4 highlights the meshing strategy and the refinement details for different computational domains.

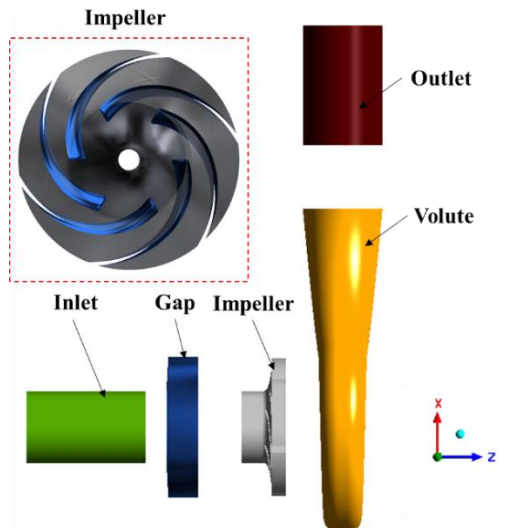


Fig. 3 Mesh generation detail of the pump model

The boundary layer mesh is essential for capturing near-wall flow and accurately reflecting flow characteristics in this region (Poppi et al., 2016). To ensure high computational accuracy, the boundary layers on the blade surface and volute tongue are refined. The y^+ value is employed to test the position of the nodes closest to the wall, ensuring adequate node density near the wall for different flow patterns. The y^+ value, a dimensionless variable, is defined as:

$$y^+ = \frac{uy}{\nu} \tag{2}$$

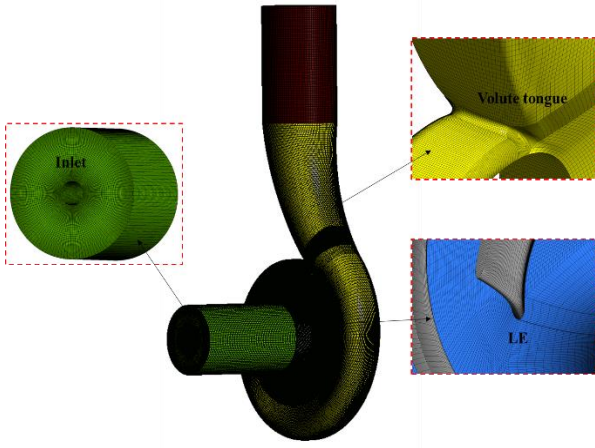


Fig. 4 Mesh details of different simulation domains

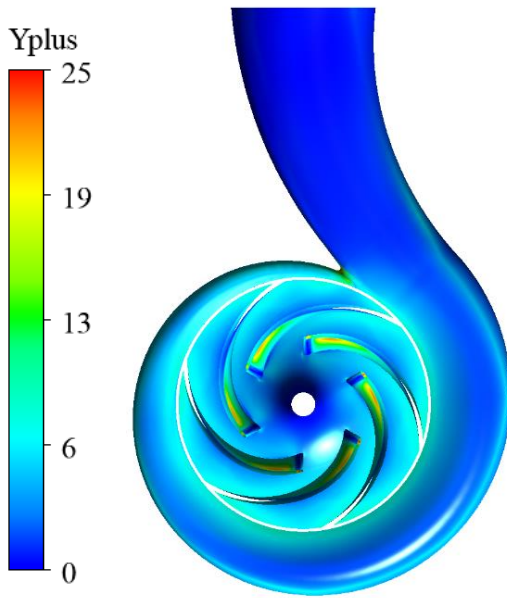


Fig. 5 Distribution of y^+ on the blade

where u represents the wall friction velocity (m/s), y is the distance between the nearest node and the wall (m), and ν denotes the kinematic viscosity (Pa·s). The y^+ values for the blade surface and volute wall are presented in Fig. 5.

2.3 Grid Independence Test

A grid independence analysis is performed to minimize solution errors due to grid size (Ji et al., 2021a). This involves using different mesh sizes and evaluating the variation in head under design conditions to select an optimal grid size for further study. The numerical convergence criterion for unsteady calculations is set to 10^{-5} .

To assess the sensitivity of computational mesh resolution, this study employs the Grid Convergence Index (GCI) method, introduced by Roache (1993) and Schleicher et al. (2015). The GCI method ensures that simulation results exhibit monotonic convergence for reliable outcomes. Three grid configurations with varying refinement levels are analyzed under the rated operating

conditions of the original impeller. This systematic approach evaluates how mesh resolution affects the accuracy and stability of simulation results. The GCI formula is provided in (Ji et al., 2020b).

$$GCI = \frac{|F_s| \alpha_{b+1,b}}{r_{b+1,b}^p - 1} \quad (3)$$

where F_s is the safety factor, taking values in the range of 1.25-3.00 and 1.25 when three or more grids are used.

r denotes the grid refinement ratio and is defined as follows:

$$r_{b+1,b} = \left(\frac{N_{b+1}}{N_b} \right)^{\frac{1}{D}} \quad (4)$$

where N is the number of control cells of the grid; D is the computational dimension; the subscript b represents different grid schemes, with a larger b value indicating a denser grid.

φ is the relative error of the results obtained from numerical calculations using two sets of grids with adjacent quantities:

$$\alpha_{b+1,b} = \left| \frac{f_b - f_{b+1}}{f_{b+1}} \right| \quad (5)$$

where f_b is the numerical discrete solution of the selected convergence parameter.

κ is the convergence accuracy. When three sets of grids are used for GCI analysis, κ can be calculated iteratively based on Eq. (6) as follows:

$$\beta = \frac{1}{\ln(r_{2,1})} \left| \ln \left(\frac{f_3 - f_2}{f_2 - f_1} \right) + g(\beta) \right| \quad (6a)$$

$$g(\beta) = \ln \left(\frac{r_{2,1}^\beta - s}{r_{3,2}^\beta - s} \right) \quad (6b)$$

$$s = \text{sgn} \left(\frac{f_3 - f_2}{f_2 - f_1} \right) \quad (6c)$$

where $g(\kappa)$ is the κ -order error term coefficient that does not vary with the grid. Notably, when $\frac{f_3 - f_2}{f_2 - f_1} < 0$, i.e.,

$s = -1$, the oscillatory iterative convergence solution is prone to occur, and then the grid needs to be replaced and recreated.

As shown in Table 2, the GCI decreases from 1.21% to 0.62% as the number of grids increases, satisfying the GCI convergence requirement of being less than 1%. Consequently, the grid density scheme is selected for grid generation across all calculation domains in the final computational model.

Table 2 GCI test with different size of grids

Mesh number/ $\times 10^6$	Relative error	GCI (%)
20.3	0.000097	1.21
23.6	0.000034	0.62
30.5		

2.4 Governing Equations and Boundary Conditions

The numerical calculation of the flow field within a centrifugal pump involves solving the governing equations, which necessitates the selection of an appropriate turbulence model with closed equations. The Reynolds-averaged Navier-Stokes (RANS) approach, utilizing time-averaged and fluctuating values to represent instantaneous flow characteristics, offers high reliability and computational efficiency, making it suitable for engineering applications (Ji et al., 2021b). Turbulence models based on the RANS equations are categorized into vortex viscosity models and Reynolds stress models. The vortex viscosity models primarily address turbulence viscosity coefficients and are further divided into zero-equation models, single-equation models, and two-equation models, with the latter being the most commonly used. The standard Reynolds stress model focuses on solving Reynolds stress transport equations. The SST (Shear Stress Transport) $k-\omega$ model employs a hybrid function combining the standard $k-\omega$ and transformed $k-\varepsilon$ models. Specifically, the standard $k-\omega$ model is applied in the near-wall region, while the transformed $k-\varepsilon$ model is used further away from the wall. By accurately predicting flow separation and turbulent shear forces, especially under adverse pressure gradients, the SST $k-\omega$ model effectively prevents excessive eddy viscosity predictions. This capability makes it particularly suitable for high-precision boundary layer simulations. Consequently, the SST $k-\omega$ model's closed control equations are used in this study to numerically simulate the internal flow field of a low-specific-speed centrifugal pump under varying operating conditions.

In the SST $k-\omega$ model, the eddy viscosity coefficient, along with the equations for turbulent kinetic energy (k) and turbulent eddy frequency (ω), are expressed

$$\frac{\partial(\rho k)}{\partial t} + \frac{\partial(\rho k u_i)}{\partial x_i} = \quad (7)$$

$$\frac{\partial}{\partial x_i} \left[\left(\mu + \frac{\mu_t}{\sigma_{k3}} \right) \frac{\partial k}{\partial x_j} \right] + P_k - \beta^* \rho k \omega$$

$$\frac{\partial(\rho \omega)}{\partial t} + \frac{\partial(\rho \omega u_i)}{\partial x_i} = \quad (8)$$

$$\frac{\partial}{\partial x_j} \left[\left(\mu + \frac{\mu_t}{\sigma_{\omega 3}} \right) \frac{\partial \omega}{\partial x_j} \right] + \alpha_3 \frac{\omega}{k} P_k - \beta_3 \rho \omega^2$$

$$+ 2(1 - F_1) \rho \frac{1}{\omega \sigma_{\omega 2}} \frac{\partial k}{\partial x_j} \frac{\partial \omega}{\partial x_j}$$

$$\mu_t = \rho \frac{a_1 k}{\max(a_1 \omega, SF_2)} \quad (9)$$

$$P_k = \mu_t \left(\frac{\partial u_i}{\partial x_j} + \frac{\partial u_j}{\partial x_i} \right) \frac{\partial u_i}{\partial x_j} \quad (10)$$

$$- \frac{2}{3} \frac{\partial u_k}{\partial x_k} \left(3\mu_t \frac{\partial u_k}{\partial x_k} + \rho k \right)$$

where F_1 and F_2 function as blending factors within the model, while S represents the shear force constant. The empirical constants β and a_1 are set to 0.09 and specific values, respectively. The turbulent eddy frequency (ω) is expressed in s^{-1} , and the turbulent kinetic energy (k) in m^2/s^2 . These parameters collectively enhance the model's ability to represent and predict flow dynamics within the two-equation framework.

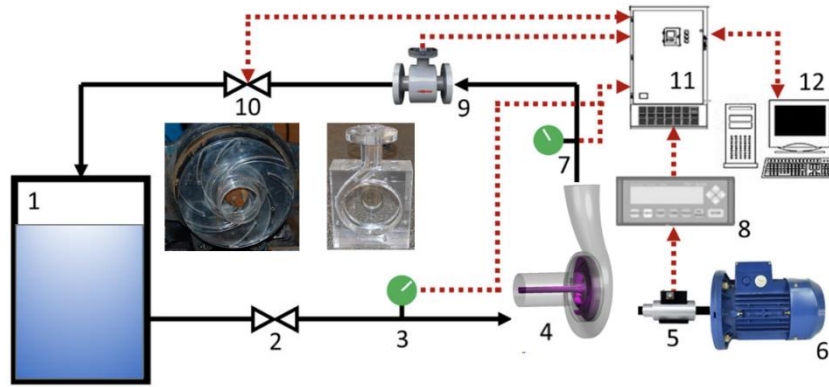
The accuracy of the simulation is heavily influenced by the boundary conditions. For steady-state conditions, the inlet boundary is defined as total pressure, while the outlet boundary is set to mass flow. The impeller is modeled as a frozen rotor when interacting with both the inlet section and the volute, with a rotation angle of 360° . The model undergoes 2500 steady-state calculation steps. For unsteady-state simulations, the inlet and outlet boundary conditions remain the same as those in the steady-state setup. However, the impeller wall is modeled with instantaneous rotation. The impeller's inlet and the contact surface between the volute and impeller are set to instantaneous frozen rotor conditions, with a total time of 0.103448 s and a time step of $t = 1.72414 \times 10^{-3}$ s, ensuring the impeller rotates five times. Each time step corresponds to a 3° rotation of the impeller. To ensure convergence, a criterion of 10^{-4} is applied to both the continuity and momentum equations.

3 EXPERIMENTAL SETUP

3.1 Experimental Equipment

The pump's performance was evaluated using the open test bench at the Zhenjiang Machinery Industry Testing Institution. Figure 6 illustrates the test bench layout. The motor was initially operated under no-load conditions to calibrate torque at the rated speed. The motor was then connected to the test pump shaft, and the necessary test devices and instruments were installed according to standard procedures. The test pipeline was filled with water at ambient temperature, and preliminary checks were conducted to ensure the proper functioning of instruments and equipment. Air was purged from the pipeline by opening the vent. Before starting the mixed-flow pump, the inlet and outlet valves were fully opened, and the motor speed was adjusted using a frequency converter to maintain a constant rated speed of 1450 rpm.

To ensure optimal experimental accuracy, the inlet valve should remain fully open while the outlet valve is gradually closed. This allows parameter measurements under varying flow conditions. Monitor the indicator on the pump's parameter measurement instrument and the system analysis program. When the indicator stabilizes at a specific value or fluctuates within a narrow range, record this as the measured value. After completing data collection for the minimum flow condition, adjust the variable frequency regulator to gradually reduce the speed



1. Water tank; 2. Valve, 3. Inlet pressure transmitter, 4. Pump; 5. Torque sensor, 6. Motor, 7. Outlet pressure transmitter, 8. Torque speed transmitter, 9. Flowmeter, 10. Valve, 11. Data acquisition terminal; 12. Computer

Fig. 6 Schematic of the experiment system

Table 3 Calculation of uncertainty

Parameter		Q	H	n
Unit		m^3/h	m	r/min
Test number	1	87.5	11.8	1446
	2	88.2	12.2	1447
	3	88.1	12.1	1451
Random uncertainty	U_{ran} (%)	0.0047	0.0044	0.0035
System uncertainty	U_{sys} (%)	0.024	0.036	0.054
Overall uncertainty	Overall uncertainty U (%)	0.0245	0.0569	0.0541
Extended overall uncertainty U_{ext} (%)		0.0822		

to zero. Once the system is fully shut down and water flow in the pipeline ceases, reopen the outlet valve fully. To minimize random errors and enhance the reliability of test data, the energy characteristic values from three repeated tests are averaged to obtain the final test result.

3.2 Uncertainty Analysis

The experiment's uncertainty analysis is determined by the square root of the quadratic sum of individual uncertainty components.

$$U = U_{sys} + U_{ran} \quad (11)$$

The random uncertainty (U_{ran}) is calculated using the Bessel method, while the systematic uncertainty (U_{sys}) is determined using a general coefficient.

Table 3 presents the detailed uncertainty calculations under the design flow condition, with the overall uncertainty calculated at 0.0822%. This indicates that the experiment satisfies the required accuracy standards.

3.3 Verification of Simulation

The pump's data acquisition terminal and processing program compute the head of the test pump using inlet and outlet pressure data from the test pipeline. Shaft power is derived from torque and speed measurements, and efficiency is calculated based on head and shaft power. The following key expressions are used:

$$H = Z_2 - Z_1 + \left(\frac{p_2 - p_1}{\rho g} \right) + \left(\frac{v_2^2 - v_1^2}{2g} \right) \quad (12)$$

$$P = \frac{n \cdot (M - M_0)}{9552} \quad (13)$$

$$\eta = \frac{\rho g Q H}{1000 P} \times 100\% \quad (14)$$

where p_1 and p_2 are, respectively, pump inlet and outlet pressures, Pa; Z_1 and Z_2 are the installation heights of the pump inlet and outlet, respectively, m. In this test, the installation heights of the pump inlet and outlet are the same; therefore, $Z_1 = Z_2$; v_1 and v_2 are, respectively, the average flow rate of the inlet and outlet of the pump, m/s, which can be calculated from the inner diameters of the inlet and outlet pipeline; M is the measured torque of the pump set, M_0 is the no-load torque, N·m; n is the speed, r/min; Q is the flow rate, m^3/h ; H is the head, m; P is the shaft power of the mixed flow pump, kW.

Figure 7 illustrates the performance curves from numerical simulations and experimental tests. The trends for head and efficiency show close agreement between numerical and experimental data. The maximum efficiency of the centrifugal pump occurs around $Q = 95 m^3/h$, marking its optimal operating point. As flow decreases, the head curve rises steadily. At $Q = 45 m^3/h$, a local minimum on the lift curve indicates a stall condition, but the reduction in lift is minimal, implying that flow

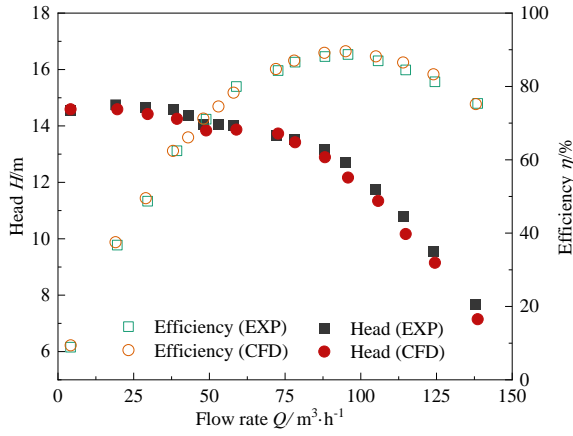


Fig. 7 Comparison of simulations and experimental results

losses are not severe. The head curve remains relatively stable at low flow conditions, suggesting a consistent flow structure within the pump. The error between numerical and experimental values is consistently under 10% across all flow conditions, confirming the numerical method's accuracy and feasibility.

4 ENTROPY PRODUCTION RATE

For estimating energy loss in centrifugal pumps, commonly used methods include the pressure difference method, empirical formulas, vortex dynamics theory, energy gradient theory, and entropy production theory. The latter three approaches provide detailed insights into internal energy losses through internal flow analysis and visual representation. Notably, the entropy production theory is increasingly utilized in fluid machinery studies (Feidt & Costea 2020). During pump operation, fluid viscosity leads to mechanical energy being irreversibly converted into internal fluid energy due to dissipation effects, causing flow loss. According to the second law of thermodynamics, this loss is characterized by entropy production (Ji et al., 2020a). Based on entropy production theory, the energy losses within the mixed-flow pump were evaluated effectively. The entropy production rate within the entire calculation domain can be categorized into three components: (1) direct dissipation entropy production rate \dot{S}_D''' W/(m³·K) caused by the mean velocity, (2) turbulent dissipation entropy production rate \dot{S}_D'''' W/(m³·K) caused by fluctuating velocities, and (3) wall entropy production rate \dot{S}_w'' W/(m²·K), caused by wall shear stress. The governing expression is as follows:

Direct dissipation entropy yield:

$$\dot{S}_D''' = \frac{\mu}{T} \left[\left(\frac{\partial \bar{u}}{\partial y} + \frac{\partial \bar{v}}{\partial x} \right)^2 + \left(\frac{\partial \bar{u}}{\partial z} + \frac{\partial \bar{w}}{\partial x} \right)^2 + \left(\frac{\partial \bar{v}}{\partial z} + \frac{\partial \bar{w}}{\partial y} \right)^2 \right] + 2 \frac{\mu}{T} \left[\left(\frac{\partial \bar{u}}{\partial x} \right)^2 + \left(\frac{\partial \bar{v}}{\partial y} \right)^2 + \left(\frac{\partial \bar{w}}{\partial z} \right)^2 \right] \quad (15)$$

Turbulent dissipation entropy yield:

$$\dot{S}_D'''' = \beta^* \frac{\rho \omega k}{T} \quad (16)$$

Wall entropy yield:

$$\dot{S}_w'' = \frac{\boldsymbol{\tau}_w \cdot \mathbf{u}_p}{T} \quad (17)$$

where \bar{u} , \bar{v} , and \bar{w} is the component of the average velocity in the x , y , and z directions, respectively, m/s; μ is the dynamic viscosity, Pa·s; The empirical coefficient $\beta=0.09$, ω is the turbulent vortex frequency; k is the turbulent kinetic energy, m²/s²; $\boldsymbol{\tau}_w$ is the wall shear stress, Pa; \mathbf{u}_p is the average velocity vector at the center of the first layer grid near the wall, m/s.

Therefore, the entropy of the mainstream region yield is

$$\dot{S}_D''' = \dot{S}_D'''' + \dot{S}_w'' \quad (18)$$

The direct dissipation entropy S_D (W/K), turbulent dissipation entropy S_D'' (W/K), and wall entropy S_w (W/K) are obtained by integrating each entropy yield in the corresponding region, as follows (Li et al., 2020):

$$S_D = \int_v \dot{S}_D''' dV \quad (19a)$$

$$S_D'' = \int_v \dot{S}_D'''' dV \quad (19b)$$

$$S_w = \int_s \dot{S}_w'' dS \quad (19c)$$

Thus, the total entropy production in the computational domain is:

$$S_D = S_D + S_D'' + S_w \quad (20)$$

5 RESULTS AND DISCUSSION

5.1 Comparison of Energy Performance

Figure 8 compares the head and efficiency curves of centrifugal pumps with and without splitter blades. The results indicate that splitter blades significantly alter pump performance, particularly under low-flow conditions. Unlike conventional impellers, whose head curves consistently exhibit a negative slope, pumps with splitter blades feature a transition from a negative to a positive slope, creating a distinct extremum point. Additionally, centrifugal pumps with splitter blades achieve higher head values compared to conventional impellers. For longer splitter blade designs, the head improvement is slightly greater, although the difference is minimal. Regarding efficiency, conventional impellers demonstrate superior performance near the design operating point. However, pumps with splitter blades achieve higher efficiency under

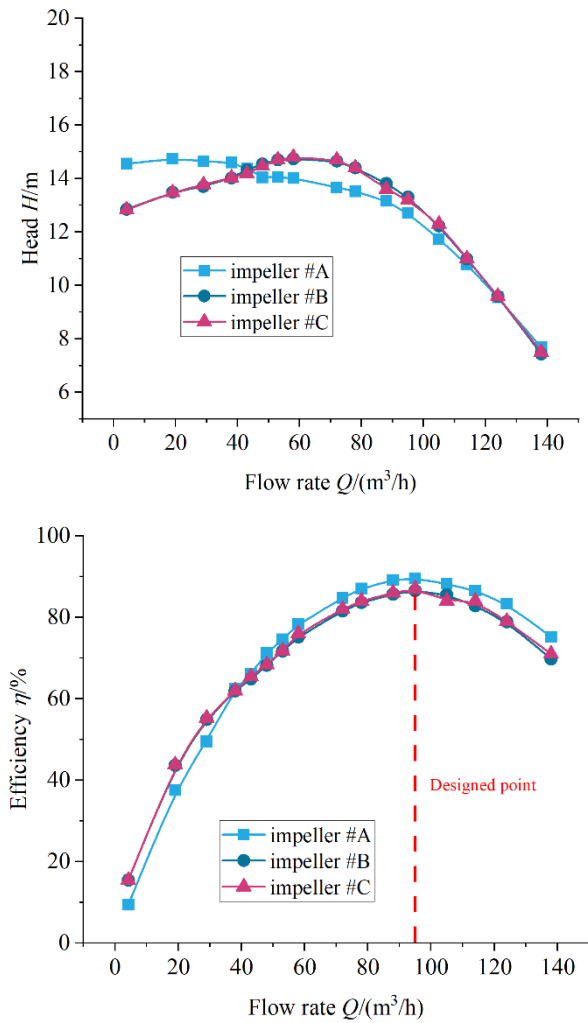


Fig. 8 Impact on the pump performance of splitter blades

low-flow conditions due to the splitter blades’ rectifying effect. This indicates that while splitter blades improve head performance, they introduce a modest efficiency trade-off at higher flow rates.

5.2 Comparison of Losses in Centrifugal Pumps Under Different Impeller Schemes

The analysis reveals that splitter blades primarily influence the performance of centrifugal pumps within a flow range of $0.4Q$ to $1.2Q$, with a particularly pronounced effect on the head curve. Figure 9 shows the total entropy generation distribution under varying flow conditions. For all impeller configurations, the entropy generation trend correlates with flow rate, decreasing initially and then increasing as flow rises. The minimum entropy generation occurs near the optimal design point, reflecting minimal internal flow losses. Due to the oversized flow design used in this study, the optimal operating point slightly deviates from the design point. At $Q=95\text{m}^3/\text{h}$ —just above the design point—entropy generation reaches its minimum, indicating the least internal losses. When comparing configurations, pumps with splitter blades demonstrate significantly lower entropy generation under low-flow conditions than those without them. However, this trend reverses at high flow rates, consistent with the observed

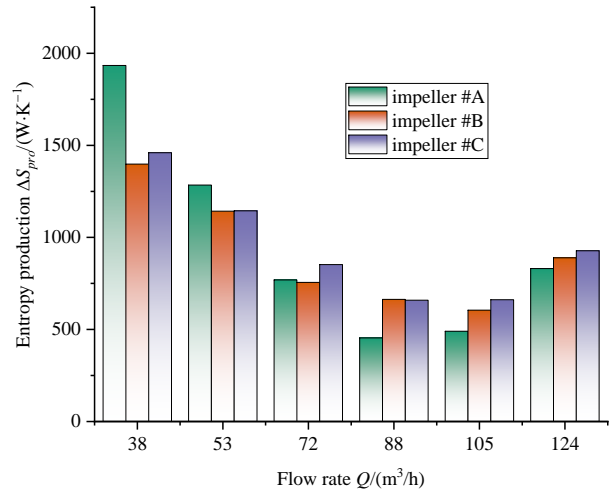


Fig. 9 Distribution of total entropy production in the centrifugal pump under different flow conditions

head and efficiency curves. Thus, splitter blades play a crucial role in enhancing both head and efficiency characteristics, extending the operational range for achieving high head or high efficiency.

To better understand the primary contributors to energy loss within centrifugal pumps, the total entropy generation distributions across various computational regions—namely, the inlet, impeller, clearance, volute, and outlet—were analyzed under three flow conditions: design ($88\text{ m}^3/\text{h}$), small-flow ($72\text{ m}^3/\text{h}$), and large-flow ($105\text{ m}^3/\text{h}$), as shown in Fig. 10. The results reveal that, across all conditions, the impeller, clearance, and volute regions experience the most severe flow losses, consistent with established fluid mechanics principles. The impeller imparts energy to the fluid, the volute facilitates energy conversion, and the clearance region, where rotor-stator interactions occur, serves as a transition zone prone to vortex formation. In contrast, the inlet and outlet regions exhibit significantly lower total entropy generation—an order of magnitude lower than that observed in the impeller, clearance, and volute regions—due to their minimal vortex activity. Under the design condition, the combined total entropy generation in the impeller and clearance regions reaches approximately 350 W/K , the highest among all regions. Centrifugal pumps equipped with splitter blades display higher entropy generation in these regions compared to those without, resulting in reduced efficiency. This trend persists under large-flow conditions. However, under small-flow conditions, the clearance region surpasses the impeller in total entropy generation, highlighting intensified flow losses driven by rotor-stator interactions. The primary cause of elevated flow losses under small-flow conditions can be traced to altered flow behavior within the impeller.

5.3 Influence Mechanism of Different Blade Structures on The Flow Structure

To further explore how different impeller structures influence flow losses, an in-depth analysis of the internal flow field was conducted, with entropy generation distributions shown in Fig. 11. The results reveal significant variation in entropy generation across impeller

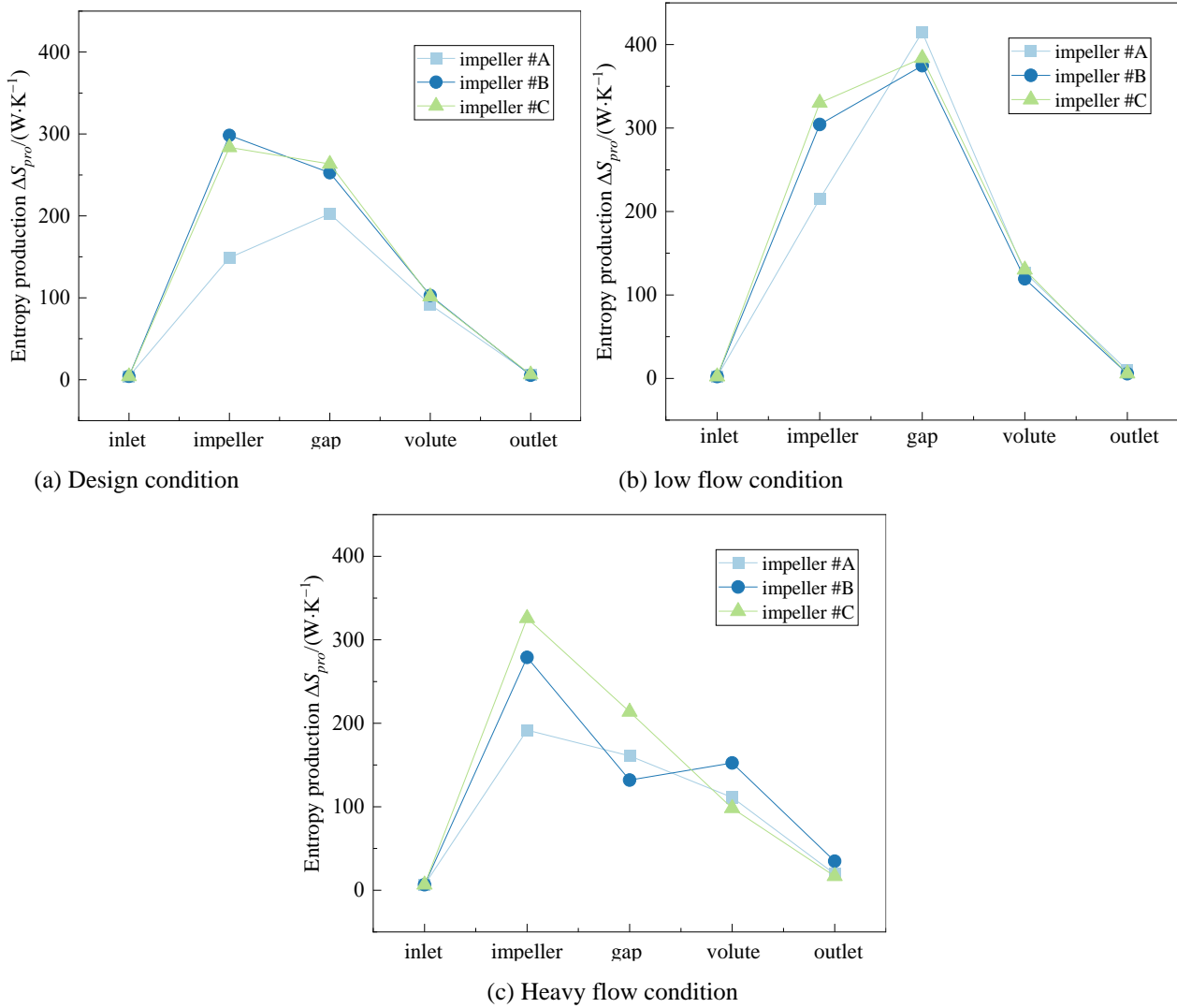
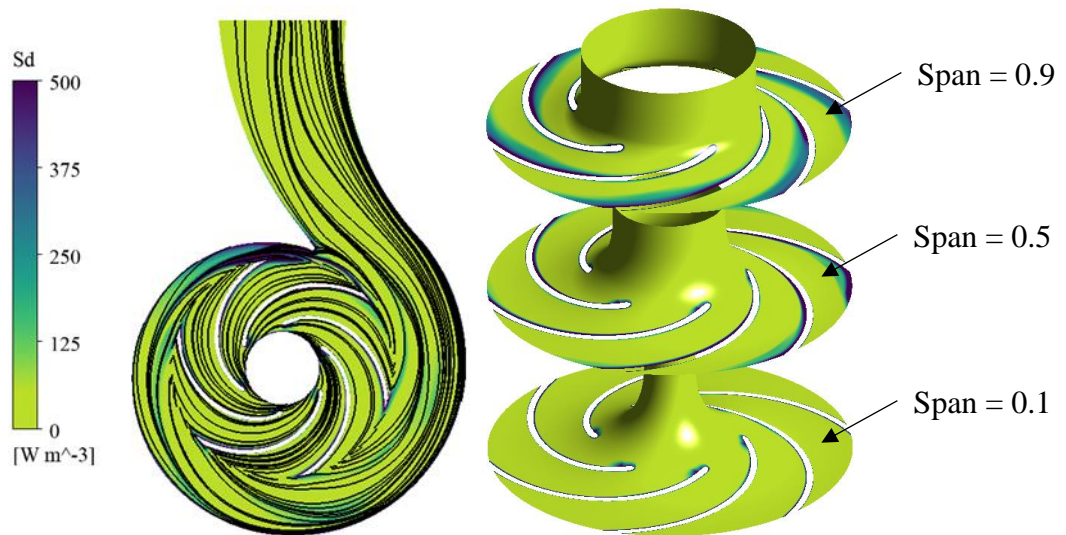


Fig. 10 Distribution of total entropy production in different computational domains

passages depending on blade structure. Under design conditions, high-entropy regions concentrate on the suction side of the blades, with particularly high values near the volute tongue. This pattern persists for impellers with splitter blades, where an additional high-entropy zone emerges in the splitter blade passage near the volute. Interestingly, this phenomenon is not dependent on the length of the splitter blades but instead correlates with their rotational angle. As the passage rotates past the volute tongue, the high-entropy zone reappears consistently in subsequent impeller passages. Furthermore, for impellers with splitter blades, entropy generation near the front and rear shrouds significantly increases due to enhanced kinetic energy transfer. Splitter blades impart greater kinetic energy to the fluid, resulting in higher flow velocities within the impeller passages compared to conventional designs. This increased velocity contributes to the observed rise in pump head. Figure 12 presents the area-averaged entropy generation distribution along the streamwise direction, with the calculation methodology detailed in Wu et al. (2022). The results highlight consistently high entropy generation near the impeller outlet for all blade configurations. However, in designs featuring splitter blades, a secondary peak

emerges near the blade inlet, signifying a major source of additional entropy generation within the impeller.

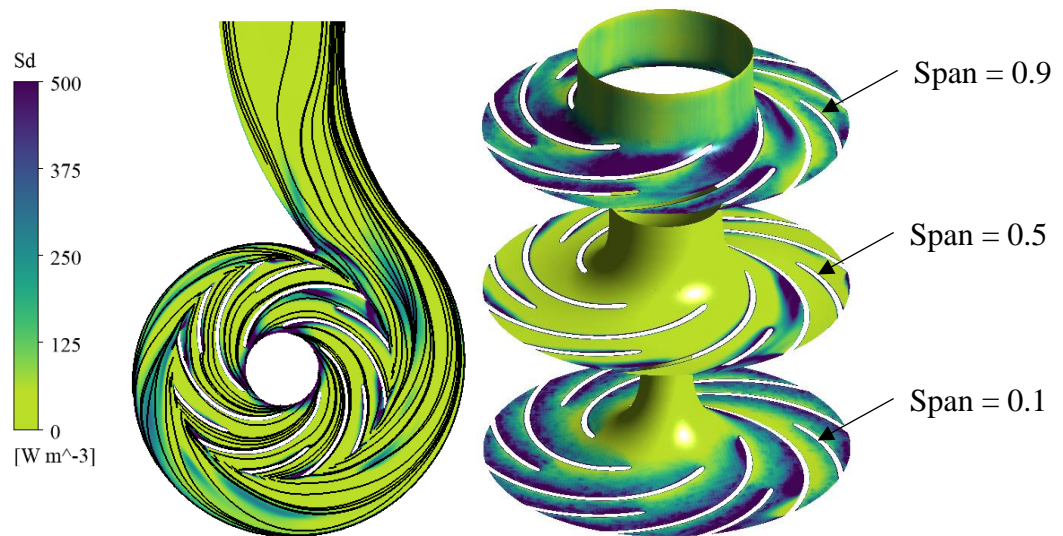
The entropy generation distribution across different volute sections was also evaluated for varying impeller structures, as illustrated in Fig. 13. Since the volute is not the dominant source of flow losses, only a qualitative analysis was performed. The analysis shows that when fluid exits the impeller and enters the volute, it undergoes a transformation from kinetic energy to potential energy. Near the rotor-stator interaction region close to the impeller outlet, dense vortex structures lead to substantial energy losses and high entropy generation. However, as the fluid progresses downstream through the volute, these high-entropy zones gradually diminish, indicating improved flow organization. For pumps with splitter blades, the high-entropy regions within the volute’s circumferential passages are more pronounced compared to those with standard impellers. This can be attributed to the continuous work exerted by the splitter blades, which results in slightly higher outlet velocities. Consequently, during the conversion of kinetic to potential energy, the fluid’s elevated kinetic energy leads to greater energy losses, thereby increasing overall entropy generation.



(a) Impeller #A



(b) Impeller #B



(c) Impeller #C

Fig. 11 Distribution of entropy production at different positions of the impeller under design conditions (left: Middle section; Right: turbo surface)

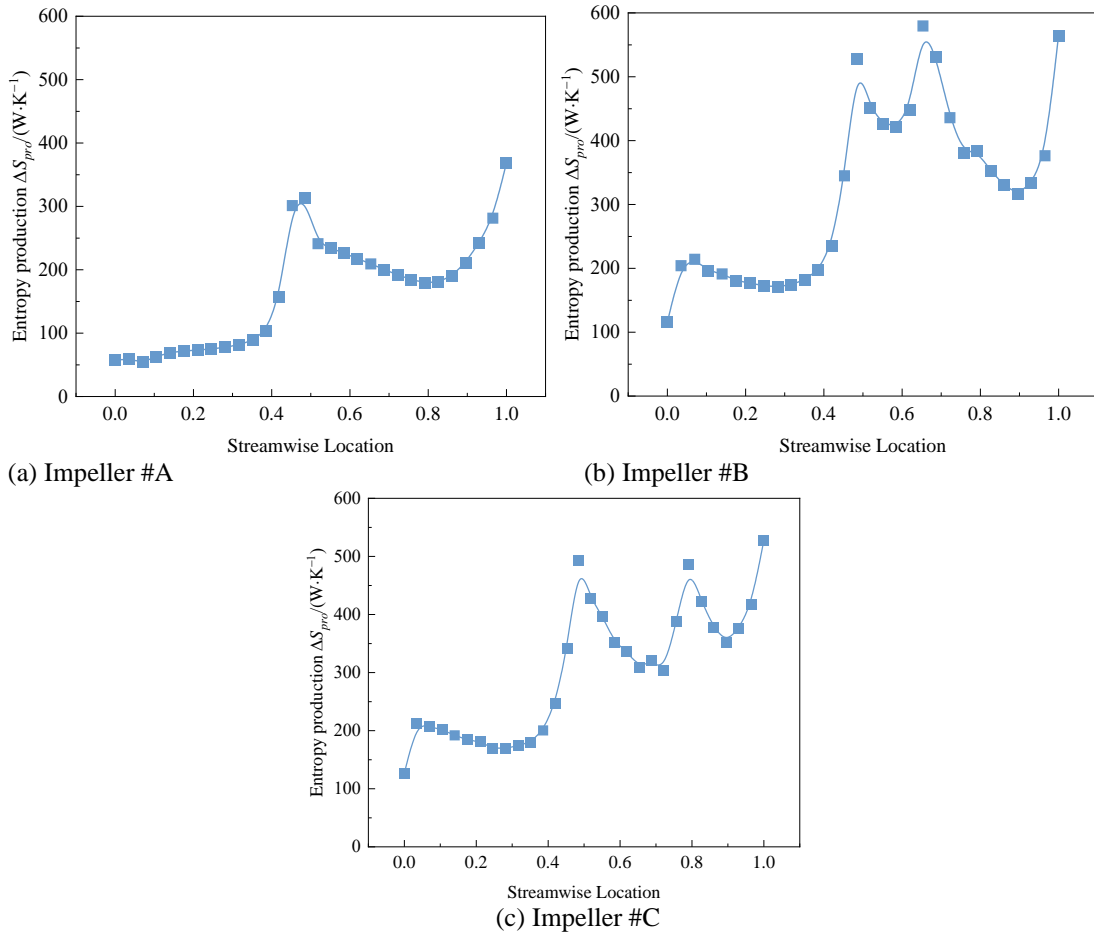


Fig. 12 Distribution of impeller flow position entropy output value under design conditions

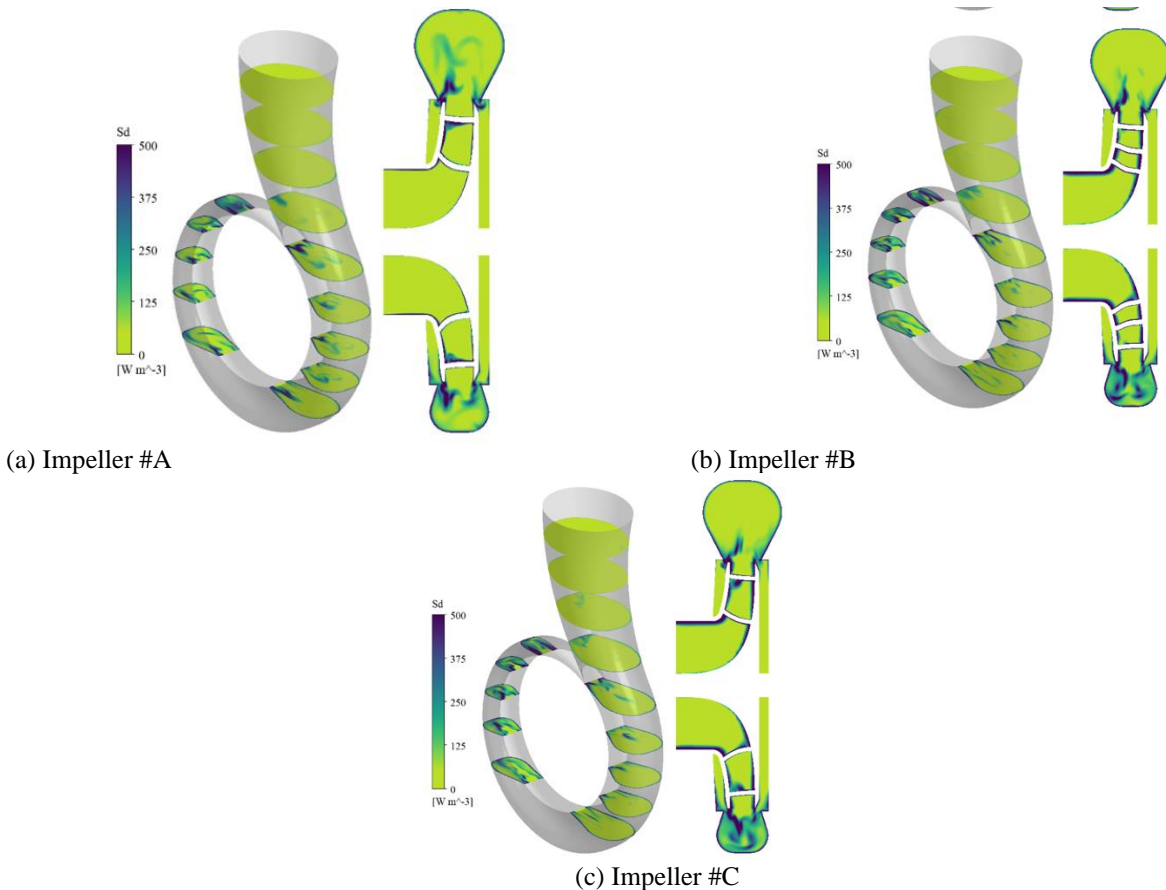


Fig. 13 Distribution of entropy production at different positions of volute under design conditions (left: cross-section; Right: longitudinal section)

In summary, splitter blade structures can improve the head performance of centrifugal pumps within specific operating ranges but at the expense of reduced efficiency. This trade-off is primarily attributed to kinetic energy losses within the impeller and volute, as well as the structural design of the splitter blades. A comparative analysis of splitter blade lengths highlights their significant influence on overall pump performance, particularly in the flow field near the impeller outlet. Future research could focus on optimizing splitter blade configurations using parametric modeling and intelligent optimization algorithms to enhance the performance of centrifugal pumps.

6 CONCLUSIONS

(1) Pumps equipped with splitter blades exhibit notable performance differences compared to conventional impeller pumps, especially at low flow rates. The head curve of pumps with splitter blades reveals a distinct extremum and a positive slope in the low-flow region. While traditional impeller designs achieve higher efficiency near their design points, the rectifying effect of splitter blades enables these impellers to perform more efficiently under low-flow conditions.

(2) In low-flow operating ranges, centrifugal pumps with splitter blades experience significantly lower total entropy generation compared to those without them. This indicates that splitter blades contribute to improving both head and efficiency, effectively broadening the operating range for achieving high head or high efficiency.

(3) The impeller, gap, and volute regions are the primary zones where flow losses occur in the pump. Under low-flow conditions, total entropy generation in the gap region surpasses that of the impeller, reflecting increased flow losses within the rotor-stator interaction zones and front-rear gaps. Although the splitter blade design enhances the head performance of centrifugal pumps within certain operating ranges, this improvement is accompanied by a reduction in efficiency. This trade-off is closely linked to kinetic energy losses within the impeller and volute, as well as the structural characteristics of the splitter blades.

ACKNOWLEDGMENTS

The work was sponsored by the Science and Technology Plan Project of Chuzhou (2024CX007) and Research Initiation Fund Project of Chuzhou University (2023qd21).

CONFLICT OF INTEREST

The authors declared that they have no conflicts of interest to this work.

AUTHORS' CONTRIBUTIONS

Qijiang Ma: Writing and editing, Software, Conceptualization. **Zhenbo Liu:** Writing and editing, Supervision. **Sen Jiang:** Writing and editing.

REFERENCES

- Chabannes, L., Štefan, D., & Rudolf, P. (2021). Effect of splitter blades on performances of a very low specific speed pump. *Energies*, 14(13), 3785. <https://doi.org/10.3390/en14133785>
- Clark, C. J., Pullan, G., Curtis, E., & Goenaga, F. (2017). Secondary flow control in low aspect ratio vanes using splitters. *Journal of Turbomachinery*, 139(9), 091003. <https://doi.org/10.1115/1.4036190>
- Djebedjian, B. O. (2020). Theoretical model to predict the performance of centrifugal pump equipped with splitter blades (Dept.M). *MEJ. Mansoura Engineering Journal*, 34(2), 50-70. <https://doi.org/10.21608/bfemu.2020.126166>
- Dong, G., Luo, Z., Guo, T., Zhang, X., Shan, R., & Dai, L. (2024). The splitter blade pump–turbine in pump mode: The hump characteristic and hysteresis effect flow mechanism. *Processes*, 12(2), 324. <https://doi.org/10.3390/pr12020324>
- Fatahian, E., Ismail, F., Ishak, M. H. H., & Chang, W. S. (2022). The role of wake splitter deflector on performance enhancement of Savonius wind turbine. *Physics of Fluids*, 34(9), 095111. <https://doi.org/10.1063/5.0111568>
- Feidt, M., & Costea, M. (2020). Effect of machine entropy production on the optimal performance of a refrigerator. *Entropy*, 22(9), 913. <https://doi.org/10.3390/e22090913>
- Gölcü, M., Usta, N., & Pancar, Y. (2007). Effects of splitter blades on deep well pump performance. *Journal of Energy Resources Technology*, 129(3), 169-176. <https://doi.org/10.1115/1.2748810>
- Gu, Y., Sun, H., Wang, C., Lu, R., Liu, B., & Ge, J. (2024). Effect of trimmed rear shroud on performance and axial thrust of multi-stage centrifugal pump with emphasis on visualizing flow losses. *Journal of Fluids Engineering*, 146(1). <https://doi.org/10.1115/1.4063438>
- Hu, J., Zhao, Z., He, X., Zeng, W., Yang, J., & Yang, J. (2023). Design techniques for improving energy performance and S-shaped characteristics of a pump-turbine with splitter blades. *Renewable Energy*, 212, 333-349. <https://doi.org/10.1016/j.renene.2023.05.074>
- Ji, L., He, S., Li, W., Shi, W., Li, S., Li, H., & Agarwal, R. (2023). Exploration of blade thickness in suppressing rotating stall of mixed flow pump. *Arabian Journal for Science and Engineering*, 48(6), 8227-8251. <https://doi.org/10.1007/s13369-023-07901-x>
- Ji, L., Li, W., Shi, W., & Agarwal, R. K. (2021a). Application of Wray–Agarwal turbulence model in flow simulation of a centrifugal pump with semi-spiral suction chamber. *Journal of Fluids Engineering*, 143(3), 031203.

- <https://doi.org/10.1115/1.4049050>
- Ji, L., Li, W., Shi, W., Chang, H., & Yang, Z. (2020a). Energy characteristics of mixed-flow pump under different tip clearances based on entropy production analysis. *Energy*, *199*, 117447. <https://doi.org/10.1016/j.energy.2020.117447>
- Ji, L., Li, W., Shi, W., Tian, F., & Agarwal, R. (2020b). Diagnosis of internal energy characteristics of mixed-flow pump within stall region based on entropy production analysis model. *International Communications in Heat and Mass Transfer*, *117*, 104784. <https://doi.org/10.1016/j.icheatmasstransfer.2020.104784>
- Ji, L., Li, W., Shi, W., Tian, F., & Agarwal, R. (2021b). Effect of blade thickness on rotating stall of mixed-flow pump using entropy generation analysis. *Energy*, *236*, 121381. <https://doi.org/10.1016/j.energy.2021.121381>
- Ji, L., Pu, W., Li, W., Shi, W., Tian, F., Yang, Y., & Agarwal, R. (2024). Flow instability in mixed-flow/axial-flow pump: A review of relationship between tip leakage flow distortion and rotating stall. *Proceedings of the Institution of Mechanical Engineers, Part A: Journal of Power and Energy*. <https://doi.org/10.1177/09576509241287838>
- Jin, F., Luo, Y., Zhao, Q., Cao, J., & Wang, Z. (2023). Energy loss analysis of transition simulation for a prototype reversible pump turbine during load rejection process. *Energy*, *284*, 129216. <https://doi.org/10.1016/j.energy.2023.129216>
- Kergourlay, G., Younsi, M., Bakir, F., & Rey, R. (2007). Influence of splitter blades on the flow field of a centrifugal pump: test-analysis comparison. *International Journal of Rotating Machinery*, *2007*(1), 085024. <https://doi.org/10.1155/2007/85024>
- Khalafallah, M. G., Saleh, H. S., Ali, S. M., & Abdelkhalek, H. M. (2021). CFD investigation of flow through a centrifugal compressor diffuser with splitter blades. *Journal of Engineering and Applied Sciences*, *68*, 1-23. <https://doi.org/10.1186/s44147-021-00040-w>
- Li, W., Huang, Y., Ji, L., Ma, L., Agarwal, R. K., & Awais, M. (2023). Prediction model for energy conversion characteristics during transient processes in a mixed-flow pump. *Energy*, *271*, 127082. <https://doi.org/10.1016/j.energy.2023.127082>
- Li, W., Li, E., Ji, L., Zhou, L., Shi, W., & Zhu, Y. (2020). Mechanism and propagation characteristics of rotating stall in a mixed-flow pump. *Renewable Energy*, *153*, 74-92. <https://doi.org/10.1016/j.renene.2020.02.003>
- Li, W., Li, H., Liu, M., Ji, L., Agarwal, R. K., & Jin, S. (2024a). Energy dissipation mechanism of tip-leakage cavitation in mixed-flow pump blades. *Physics of Fluids*, *36*(1), 015115. <https://doi.org/10.1063/5.0183540>
- Li, W., Yang, Q., Yang, Y., Ji, L., Shi, W., & Agarwal, R. (2024b). Optimization of pump transient energy characteristics based on response surface optimization model and computational fluid dynamics. *Applied Energy*, *362*, 123038. <https://doi.org/10.1016/j.apenergy.2024.123038>
- Liang, Z., Wang, J., Jiang, B., Zhou, H., Yang, W., & Ling, J. (2023). Large-eddy simulation of flow separation control in low-speed diffuser cascade with splitter blades. *Processes*, *11*(11), 3249. <https://doi.org/10.3390/pr11113249>
- Miyamoto, H., Nakashima, Y., & Ohba, H. (1992). Effects of splitter blades on the flows and characteristics in centrifugal impellers. *JSME International Journal. Ser. 2, Fluids Engineering, Heat Transfer, Power, Combustion, Thermophysical Properties*, *35*(2), 238-246. https://doi.org/10.1299/jsmeb1988.35.2_238
- Miyamoto, H., Nakashima, Y., Yasunaga, Y., & Shiramoto, K. (1989a). Study on flow of centrifugal impeller: 1st report, flow measurement in unshrouded impeller passage. *Transactions of the Japan Society of Mechanical Engineers (in Japanese)*, *55*(512B), 1137-1141. <https://doi.org/10.1299/kikaib.55.1137>
- Miyamoto, H., Nakashima, Y., Yasunaga, Y., & Shiramoto, K. (1989b). Study on flow of centrifugal impeller: 2nd report, flow measurement in shrouded impeller passage. *Transactions of the Japan Society of Mechanical Engineers (in Japanese)*, *55*(518B), 3108-3112. <https://doi.org/10.1299/kikaib.55.3108>
- Namazizadeh, M., Talebian Gevari, M., Mojaddam, M., & Vajdi, M. (2020). Optimization of the splitter blade configuration and geometry of a centrifugal pump impeller using design of experiment. *Journal of Applied Fluid Mechanics*, *13*(1), 89-101. <https://doi.org/10.29252/jafm.13.01.29856>
- Poppi, S., Bales, C., Haller, M. Y., & Heinz, A. (2016). Influence of boundary conditions and component size on electricity demand in solar thermal and heat pump combisystems. *Applied Energy*, *162*, 1062-1073. <https://doi.org/10.1016/j.apenergy.2015.10.190>
- Pu, W., Ji, L., Li, W., Shi, W., Tian, F., Xiao, C., Yang, Q., Yang, Y., & Agarwal, R. (2024a). Study on the particle dynamic characteristics in a centrifugal pump based on an improved computational fluid dynamics-discrete element model. *Physics of Fluids*, *36*(12), 123331. <https://doi.org/10.1063/5.0242078>
- Pu, W., Ji, L., Li, W., Yang, Q., Liu, Z., Yang, Y., Li, H., Huang, W., & Agarwal, R. (2024b). Experimental study on the unsteady evolution mechanism of centrifugal pump impeller wake under solid-liquid two-phase conditions: Impact of particle concentration. *Physics of Fluids*, *36*(11), 113327. <https://doi.org/10.1063/5.0239240>
- Roache, P. J. (1993). American society of mechanical engineers. fluids engineering division. quantification of uncertainty in computational fluid dynamics. *American Society of Mechanical Engineers*, *29*(1), 123-60.

<https://doi.org/10.1146/annurev.fluid.29.1.123>.

- Schleicher, W. C., Riglin, J. D., & Oztekin, A. (2015). Numerical characterization of a preliminary portable micro-hydrokinetic turbine rotor design. *Renewable Energy*, 76, 234-241. <https://doi.org/10.1016/j.renene.2014.11.032>
- Shigemitsu, T., Fukutomi, J., Wada, T., & Shinohara, H. (2013). Performance analysis of mini centrifugal pump with splitter blades. *Journal of Thermal Science*, 22(6), 573-579. <https://doi.org.iclibezpl.cc.ic.ac.uk/10.1007/s11630-013-0664-4>
- Siddique, M. H., Samad, A., & Hossain, S. (2022). Centrifugal pump performance enhancement: Effect of splitter blade and optimization. *Proceedings of the Institution of Mechanical Engineers, Part A: Journal of Power and Energy*, 236(2), 391-402. <https://doi.org/10.1177/09576509211037407>
- Song, H., Zhang, J., Huang, P., Cai, H., Cao, P., & Hu, B. (2020). Analysis of rotor-stator interaction of a pump-turbine with splitter blades in a pump mode. *Mathematics*, 8(9), 1465. <https://doi.org/10.3390/math8091465>
- Wang, B., Zhang, H., Deng, F., Wang, C., & Si, Q. (2020). Effect of short blade circumferential position arrangement on gas-liquid two-phase flow performance of centrifugal pump. *Processes*, 8(10), 1317. <https://doi.org/10.3390/pr8101317>
- Wu, C., Pu, K., Li, C., Wu, P., Huang, B., & Wu, D. (2022). Blade redesign based on secondary flow suppression to improve energy efficiency of a centrifugal pump. *Energy*, 246, 123394. <https://doi.org/10.1016/j.energy.2022.123394>
- Xu, Z., Kong, F., Tang, L., Liu, M., Wang, J., & Qiu, N. (2022). Effect of blade thickness on internal flow and performance of a plastic centrifugal pump. *Machines*, 10(1), 61. <https://doi.org/10.3390/machines10010061>
- Ye, L., Yuan, S., Zhang, J., & Yuan, Y. (2012). *Effects of splitter blades on the unsteady flow of a centrifugal pump*. Fluids Engineering Division Summer Meeting, Rio Grande, Puerto Rico, USA, 44755, 435-441. <https://doi.org/10.1115/FEDSM2012-72155>
- Yu, H., Wang, T., Dong, Y., Gou, Q., Lei, L., & Liu, Y. (2023). Numerical investigation of splitter blades on the performance of a forward-curved impeller used in a pump as turbine. *Ocean Engineering*, 281, 114721. <https://doi.org/10.1016/j.oceaneng.2023.114721>
- Zhang, J., Li, G., Mao, J., Yuan, S., Qu, Y., & Jia, J. (2020). Numerical investigation of the effects of splitter blade deflection on the pressure pulsation in a low specific speed centrifugal pump. *Proceedings of the Institution of Mechanical Engineers, Part A: Journal of Power and Energy*, 234(4), 420-432. <https://doi.org/10.1177/0957650919867176>
- Zhu, L., Jin, Y., Li, Y., Jin, Y., Wang, Y., & Zhang, L. (2013). Numerical and experimental study on aerodynamic performance of small axial flow fan with splitter blades. *Journal of Thermal Science*, 22(4), 333-339. <https://doi.org.iclibezpl.cc.ic.ac.uk/10.1007/s11630-013-0632-z>